PNAS RESEARCH ARTICLE | APPLIED PHYSICAL SCIENCES

Explaining and predicting the Southern Hemisphere eddy-driven jet

Julia Mindlin[a,1], Theodore G. Shepherd[b,c], Marisol Osman[d,e,f], Carolina S. Vera[d,e,f], and Marlene Kretschmer[a,b]

Affiliations are included on p. 10.

Edited by Jose A. Marengo, National Centre for Monitoring and Early Warnings of Natural Disasters, São José dos Campos, Brazil; received January 10, 2025; accepted June 8, 2025, by Editorial Board Member Mercedes Bustamante

The summertime eddy-driven jet (EDJ) in the Southern Hemisphere is a critical mediator between regional climate and large-scale phenomena, guiding synoptic systems that shape weather patterns. Uncertainties in global climate models (GCMs)-particularly in projecting changes in remote drivers like tropical warming, stratospheric polar vortex strengthening, and asymmetric tropical Pacific warming-hinder predictions of EDJ trends and associated regional outcomes. In this study, we develop a causal framework that combines observations, reanalysis datasets, and storylines estimated from the Coupled Model Intercomparison Project (CMIP) projections to attribute past EDJ changes and predict plausible future trajectories. Our findings indicate that tropical warming has evolved along the low end of plausible CMIP trajectories, while the stratospheric polar vortex shows robust strengthening, both strongly influencing observed EDJ trends. Our results suggest that 50% of the observed EDJ latitude shift can be directly attributed to global warming (GW), and the remaining 50% to remote drivers whose attribution to GW remains uncertain. Importantly, GCMs appear to accurately estimate the observed latitudinal shifts but underestimate the observed strengthening of the EDJ, while the proposed storylines are able to capture the observed trend. By integrating causal inference with climate storylines, our approach narrows the divide between attribution and prediction, offering a physically grounded method to estimate plausible pathways of future climate change.

eddy-driven jet | storylines | Southern Hemisphere | causal networks | near-term projections

Significance

Accurate climate predictions are vital for preparing for future weather and regional climate changes, helping communities and policymakers make informed decisions. The Southern Hemisphere's summertime eddy-driven jet (EDJ) strongly influences weather, yet current models disagree on its future due to uncertainties in the response of large-scale climate phenomena to anthropogenic forcing. Our study introduces a method that integrates observations with climate model projections to better understand and predict EDJ behavior. By increasing the understanding of how the tropical and the stratospheric influences are combined, and accounting for model disagreement, we reduce uncertainty in model predictions and provide more reliable near-term climate prediction, offering a pathway to evaluate and improve model ensembles.

The Southern Hemisphere's (SH) summertime eddy-driven jet (EDJ) is a critical feature of extratropical circulation that acts as a tropospheric mediator of the influence of remote drivers on regional climate (1, 2). The strength and latitudinal position of the SH EDJ in austral summer are among the circulation features with the most prominent forced response in both observations and models (3, 4). The zonal mean shift and strengthening observed in the last four decades has been attributed to ozone depletion (5–8). However, although ozone recovery is observable and zonal mean circulation trends have slowed down (9), the trends continue (3, 10) and are presenting considerable zonal asymmetries (11, 12). This is in broad agreement with predictions from model simulations (10, 13–15) that anticipate a poleward shift and a strengthening of the EDJ as a robust response to CO2 emissions (16–19). All phases of the Coupled Model Intercomparison Project (1, 10, 20, 21) project further strengthening and latitudinal shifts of the upper and lower SH westerlies for the remainder of the century.

Understanding the mechanisms that drive regional climate change is critical to improve projections and support decision-making in a rapidly warming world. General circulation models (GCMs) are indispensable tools for studying large-scale circulation responses to anthropogenic forcing. However, differences in the way that GCMs project large-scale circulation features can lead to significant variations in regional climate projections (22). The storyline approach provides a framework to infer plausible climatic changes with predictions that are conditional on the uncertain response of a few key drivers known to govern the targeted responses (23, 24). Large-scale remote drivers of the EDJ include tropical amplification of global warming, induced by tropical SST warming. This is associated with the expansion of the Hadley cell and the shift and strengthening of the extratropical storm tracks, both of which are linked to the EDJ (18, 25). This circulation change has in turn been associated with drying trends in the subtropical SH (1, 26). Another key driver is the stratospheric polar vortex, which modulates the position and trends of the SH EDJ and extratropical storm tracks (1, 27, 28), leading to increases in precipitation across mid-latitudes (1). Moreover, asymmetric warming trends

The authors declare no competing interest.

This article is a PNAS Direct Submission. J.A.M. is a guest editor invited by the Editorial Board.

[1]To whom correspondence may be addressed. Email: julia.mindlin@uni-leipzig.de.

This article contains supporting information online at https://www.pnas.org/lookup/suppl/doi:10.1073/pnas.2500697122/-/DCSupplemental.

Published July 14, 2025.

of tropical Pacific sea surface temperatures (SST) drive atmospheric teleconnections that affect multiple regions and the EDJ in the Pacific basin (12, 29). Model disagreement in SST warming patterns can lead to large differences among the projected long-term precipitation trends across the globe (26, 30, 31). Finally, responses of these remote drivers also depend on the models' transient climate sensitivity and climate sensitivity to ozone depletion and recovery (21), providing an additional source of uncertainty.

Recognizing that uncertainties in the response of these drivers imply various plausible future climates can aid decision-makers (24, 32). The description of uncertainty in terms of a few storylines is a recent advance that calls for an attempt to constrain such storylines based on the observed trends. Constraining an ensemble of future storylines of the EDJ using observations would represent a 'conditional emergent constraint' on the EDJ response. However, constraints need to be anchored in physical understanding and causal relationships to be robust (33).

Here, we use causal inference (34) to quantify the relationships between a set of well-documented large-scale drivers and the SH EDJ. We build upon previous work and only consider drivers for which storylines have already been proposed (1, 21, 30, 31). We focus on attributing EDJ trends over the period 1950–2023 and propose an approach to evaluate storylines by combining reanalysis datasets and observational products with the latest available CMIP projections. Finally, we assess whether specific ensembles of the proposed storylines can better explain the observed historical trends, as compared to the CMIP6 multimodel ensemble mean (MEM). Our approach provides the basis for a physically grounded dynamical attribution of recent EDJ changes, as well as constraints on dynamical storylines of plausible future changes. Given that model biases, for example in the jet latitude in the present climate, could influence the jet projected response (35), an assessment of plausible changes based on observed causal relationships and projected large-scale drivers offers a complementary approach to the intercomparison of model output.

Results

Causal Analysis of Remote Driver Influence on the EDJ. The proposed causal network (CN) in Fig. 1*A* represents our causal hypotheses on the relationship between anthropogenic forcings, global warming, the proposed remote drivers, and the summer EDJ in the SH. Trends in the jet forced by anthropogenic greenhouse gases and ozone depleting substances are assumed to be mediated by forced trends in the stratospheric polar vortex (SPV), SST warming in the Central (CP) and Eastern tropical Pacific (EP), and tropical warming (TW). In addition, we consider a remaining direct effect of GW, which includes mediation from other unspecified mechanisms. We use detrended ERA5 data to estimate the causal effect between the remote drivers and the EDJ at each grid point, which yields a causal map for each link (Fig. 1*B*, RD $\rightarrow$ $u850$, $\beta_i(x)$, where x represents a grid cell). To test that these estimates are robust, we quantify the causal effects over different periods and in three reanalysis products (here we only show ERA5) as well as piControl simulations (*Materials*) and report comparable results (*SI Appendix*, Figs. S1–S3 and Text S1). The only qualitative difference is found for GW $\rightarrow$ $u850$. The GW index corresponds to the global average of surface temperature, which in the reanalysis captures a poleward shift of the westerly winds, while in piControl simulations the response is an equatorward shift (See *SI Appendix*, Text S1 and Figs. S1–S5 for further discussion). This is understandable because in piControl simulations the variations in GW are driven by internal variability rather than by external forcing, whereas in observations, the linear detrending does not eliminate the forced response (*SI Appendix*, Fig. S5). The residual effect of GW after linear detrending allows us to estimate the wind response to forced changes in GW. For the remainder of the article we will consider the causal link strengths estimated from linearly detrended ERA5 data (Fig. 1*B*) as our best estimate of the wind response to the drivers.

Reconstruction and Attribution of Observed Eddy-Driven Jet Trends. The estimated causal effects can be used to evaluate the time evolution of the EDJ as a linear combination of the $u850$ response to the remote drivers' evolution $\beta_i(x) \cdot RD_i(t)$. We compute the latitude and strength of the EDJ in the zonal mean, the Pacific and the Atlantic-Indian basin for the period 1950–2023, resulting in six EDJ metrics. The trends and a large part of the internal variability are well captured by the reconstructions based on the causal drivers (black lines in the *Left* part of Fig. 2). In particular, we capture the strong shift and weak strengthening in the Atlantic-Indian basin (−0.6 deg/dec of latitude shift and 0.3 m/s/dec of strengthening in ERA5) as opposed to the smaller shift and stronger intensification over the Pacific basin (−0.33 deg/dec and 0.48 m/s/dec in ERA5), previously described by Waugh et al. (11). The relative contribution of each driver is shown in the bar plots in Fig. 2. The individual driver contributions are estimated by evaluating the trends in jet metrics from reconstructions based on one driver at a time (Fig. 2 and *Materials*). In the zonal mean, we estimate that GW has directly contributed to one-half of the observed latitude shift, and the remaining shift is explained by TW and SPV strengthening, whose attribution to GW is left open for now. We further find that the latitude shift is large over the Atlantic basin (Fig. 2*E*), while the trend in the Pacific is smaller and mainly directly controlled by GW (Fig. 2*C*). The EP warming and SPV strengthening have a secondary effect (Fig. 2*I*) for this metric. The remote drivers TW and SPV, together with GW, explain the strengthening in the Pacific basin while TW and EP warming control the strengthening in the Atlantic basin. Note that the role of ozone depletion is implicitly included in this attribution, as ozone depletion is the main driver of observed strengthening trends in the SPV (7).

To test whether the proposed CN can also reproduce modeled trends, we apply the same methodology and the same regression coefficients estimated from ERA5 (Fig. 1*B*) to reconstruct simulations of the period 1900–2099 using concatenated historical and scenario experiments from CMIP6 (*SI Appendix*, Figs. S6–S9). The reconstruction is based on the mean state and remote driver variability of the model, hence, the mean state bias in each model is preserved and the causal effect estimates are used to capture the variability around this mean state in response to changes in the drivers (*Materials* and *SI Appendix*, Text S2 and Fig. S10). We find that there is a very high correlation between the reconstructed time series based on the drivers and the raw output of the models ($r > 0.8$, *SI Appendix*, Fig. S8). Hence, the five included remote drivers are sufficient to explain, to a great extent, both the variability and the trends in both the observed and modeled SH circulation. Thus, it becomes imperative to attribute the observed remote driver trends.

Constraining the Uncertainty in GW Rate and SPV Response to Ozone Depletion. In the previous section, we attributed past changes of the EDJ to remote driver changes without

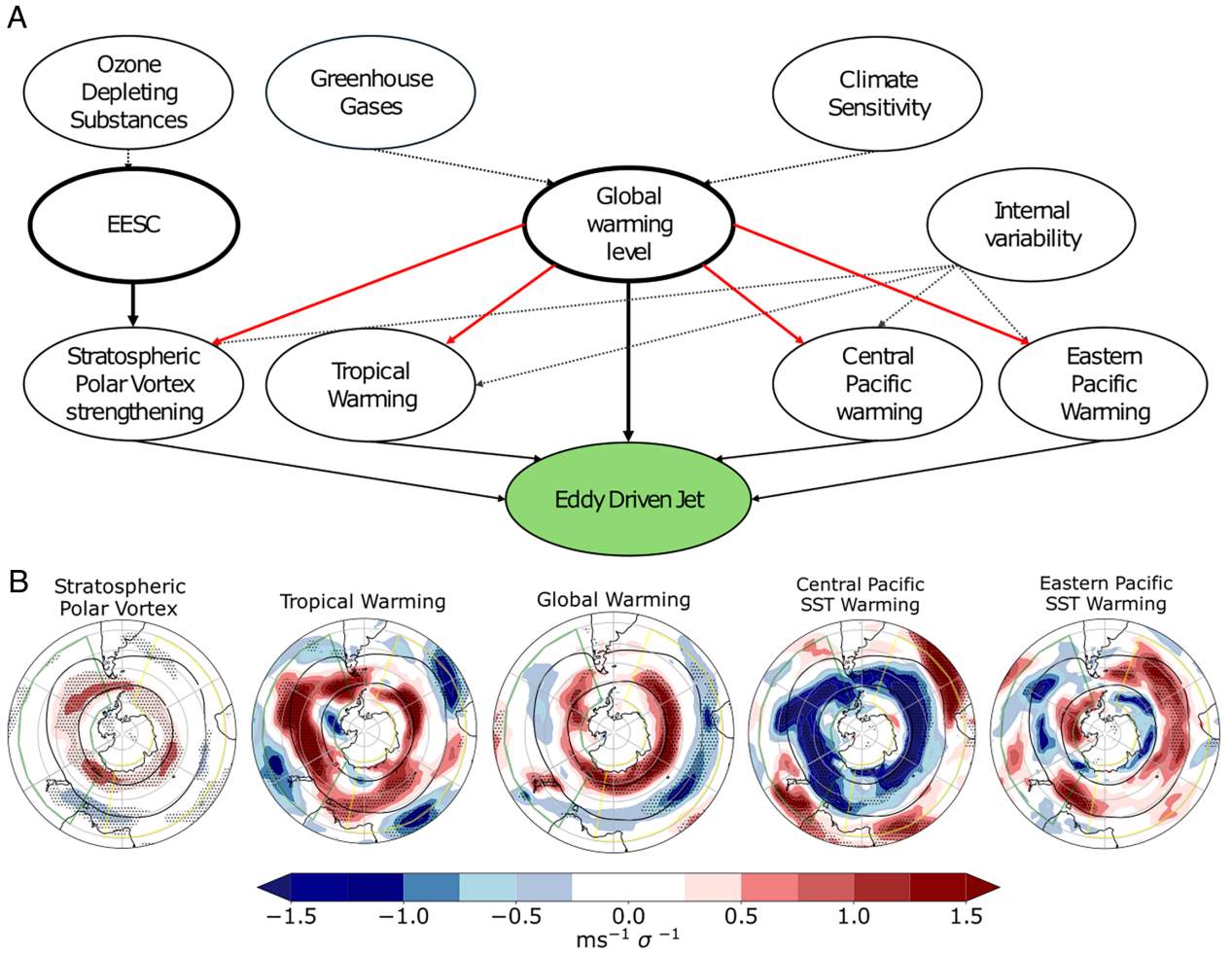

Fig. 1. (*A*) Assumed causal model for EDJ. Dashed arrows indicate the influence of internal variability on the remote drivers, red arrows indicate that trends in the remote drivers can also be forced by global warming, solid arrows indicate causal effects from the remote drivers to the EDJ at each grid cell providing a causal map for each link ($RD_i \rightarrow u850$, $\beta_i(x)$, where x represents a grid cell). (*B*) Causal maps for $u850$ estimated from detrended ERA5 reanalysis data. Stippling shows where the regression coefficients are significant above the 95% confidence level based on a Student's t test.

distinguishing between internal variability and the forced component of the remote driver trends. We now use CMIP6 simulations to evaluate plausible forced responses in the remote drivers. Each combination of plausible remote driver responses will be referred to as a dynamical storyline (23). We then use observed trends in the remote drivers to discard some of the storylines and thereby constrain the near-term projections. We do this in two steps. In the first step, we address uncertainty in the GW rate and SPV response to ozone depletion (bold nodes in Fig. 1*A*).

Under the same emissions scenario, models exhibit differences in transient climate sensitivity, leading to differences in GW rates and remote driver responses (Fig. 1*A*). Similarly, under the same concentrations of ozone-depleting substances, the SPV responds differently across models. However, we find that in the models, the SPV sensitivity to EESC (EESC → SPV) in the observed period (1979–2023) is almost perfectly correlated with the SPV sensitivity in the full period (1950–2100; Fig. 3*A*), meaning that the observed sensitivity can be used to constrain the future. As it happens, the observed sensitivity is very close to the MEM value. To isolate the role of remote driver uncertainty in shaping EDJ changes from uncertainty in transient climate sensitivity, we assess whether the GW rate in the recent past exhibits predictive skill for near-term warming rates in the model ensemble (Fig. 3*B*). We find that the observed rate of GW can be used to constrain the near-term future and that the observed GW rate (1950–2023) was very close to the MEM value. Thus, we are justified in using the MEM value for both GW and the (EESC → SPV) sensitivity, as partial emergent constraints.

To appreciate the effect of these constraints, we evaluate the remote driver spread that can be captured if high/low GW and high/low (EESC → SPV) storylines are considered. Doing so recovers the full range of remote driver responses in the CMIP6 ensemble (*SI Appendix*, Figs. S11 and S12). Hence, by conditioning on (EESC → SPV) and GW rate, we can eliminate the uncertainty arising from model uncertainty in transient climate sensitivity and in stratospheric response to ozone depletion.

Constraining Storylines of Remote Driver Sensitivity to Forcing Based on Reanalysis and Observations. We showed that causal effects of the remote drivers on the $u850$ winds can be estimated from reanalysis and observations and that the GW rate and (EESC → SPV) can be constrained by observations and reanalysis (black solid arrows in Fig. 1*A*). However, the responses of the drivers to forcing (red arrows in Fig. 1*A*) remain uncertain. As a second step to constrain this uncertainty, we first estimate plausible storylines of remote driver responses from the concatenated historical+SSP5-8.5 simulations from the CMIP6 ensemble (*SI Appendix*, Fig. S13 and Table S2 and

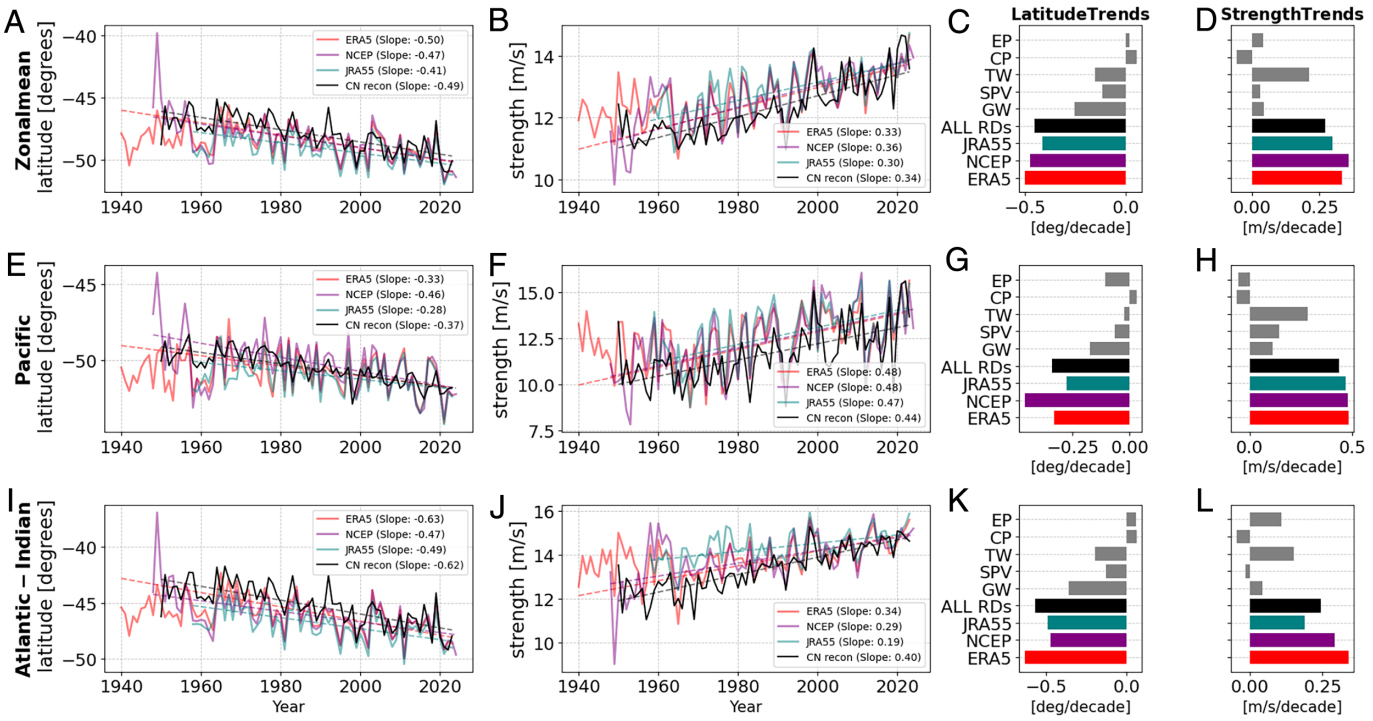

Fig. 2. Trends in EDJ metrics based on *u*850 (*Materials*) estimated in three reanalysis products (colors) and reconstructed based on evolution of its causal drivers (black). (*A*) Latitude of the zonal-mean EDJ using data from ERA5 to estimate TW and SPV and ERSSTv5 to estimate CP and EP. (*B*) Same as (*A*) but for zonal-mean EDJ strength. (*C* and *D*) Contribution of remote drivers to the total trend in zonal mean latitude and strength metrics. (*E*–*H*) Same as (*A*–*D*) but for the Pacific basin only. (*I*–*L*) Same as (*A*–*D*) but for the Atlantic-Indian basin only. Latitude and strength trends are shown in deg/decade and m/s/decade respectively.

Materials). Next, we treat each storyline as a hypothesis for the observed forced trends and we evaluate whether any of them can explain the observed trends in remote drivers better than the MEM. The modeled and observed time series of the remote drivers are shown in Fig. 4 together with the plausible storylines estimated with the historical+SSP5-8.5 simulations from the CMIP6 ensemble (*SI Appendix*, Fig. S13 and Table S2). We compare the probabilities of observing each driver's trends under the CMIP6 MEM and under a given extreme storyline. The ratio of these probabilities, called Bayes Factor (*Materials*) (36, 37), indicates whether a given storyline derived from CMIP6 models is more likely to explain the observed trends in the large-scale

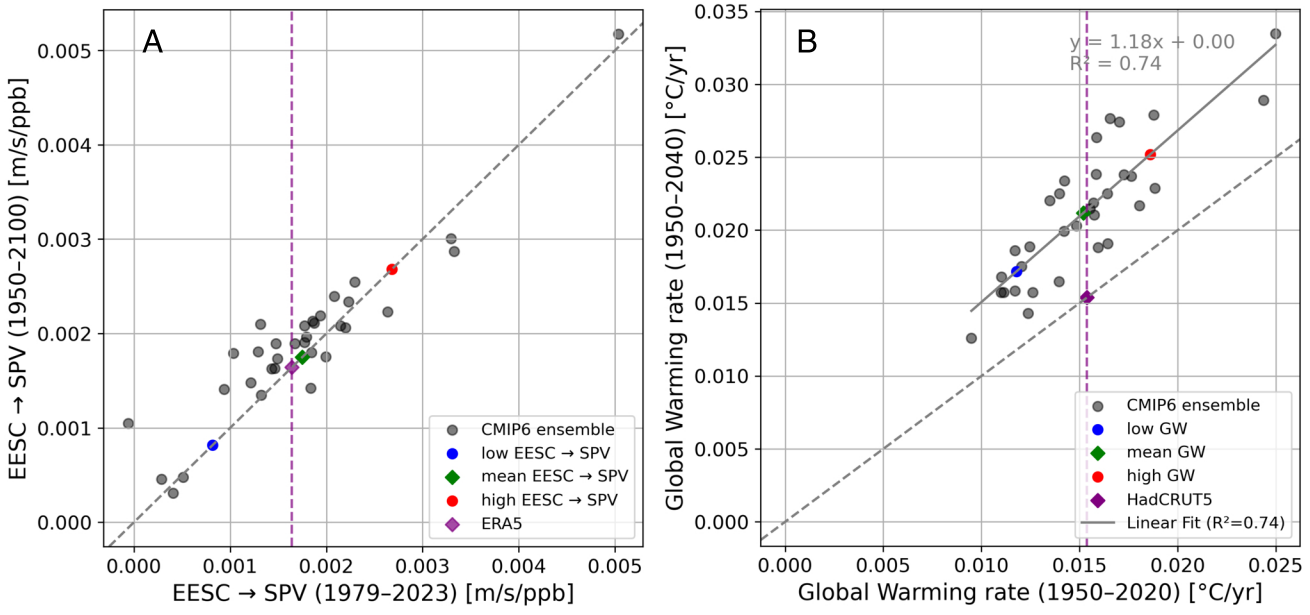

Fig. 3. (*A*) SPV sensitivity to equivalent effective stratospheric chlorine (EESC) for 1979–2023 vs. 1950–2100 in the CMIP6 ensemble, estimated via multiple linear regression with EESC and global warming (GW) as covariates. Color-coded are high (red), mean (green), and low (blue) SPV sensitivity, with ERA5 reanalysis in purple. (*B*) Rate of global mean surface temperature change for 1950–2020 vs. 1950–2040, with high (red), mean (green), and low (blue) GW storylines, and HadCRUT5 observed rates in purple.

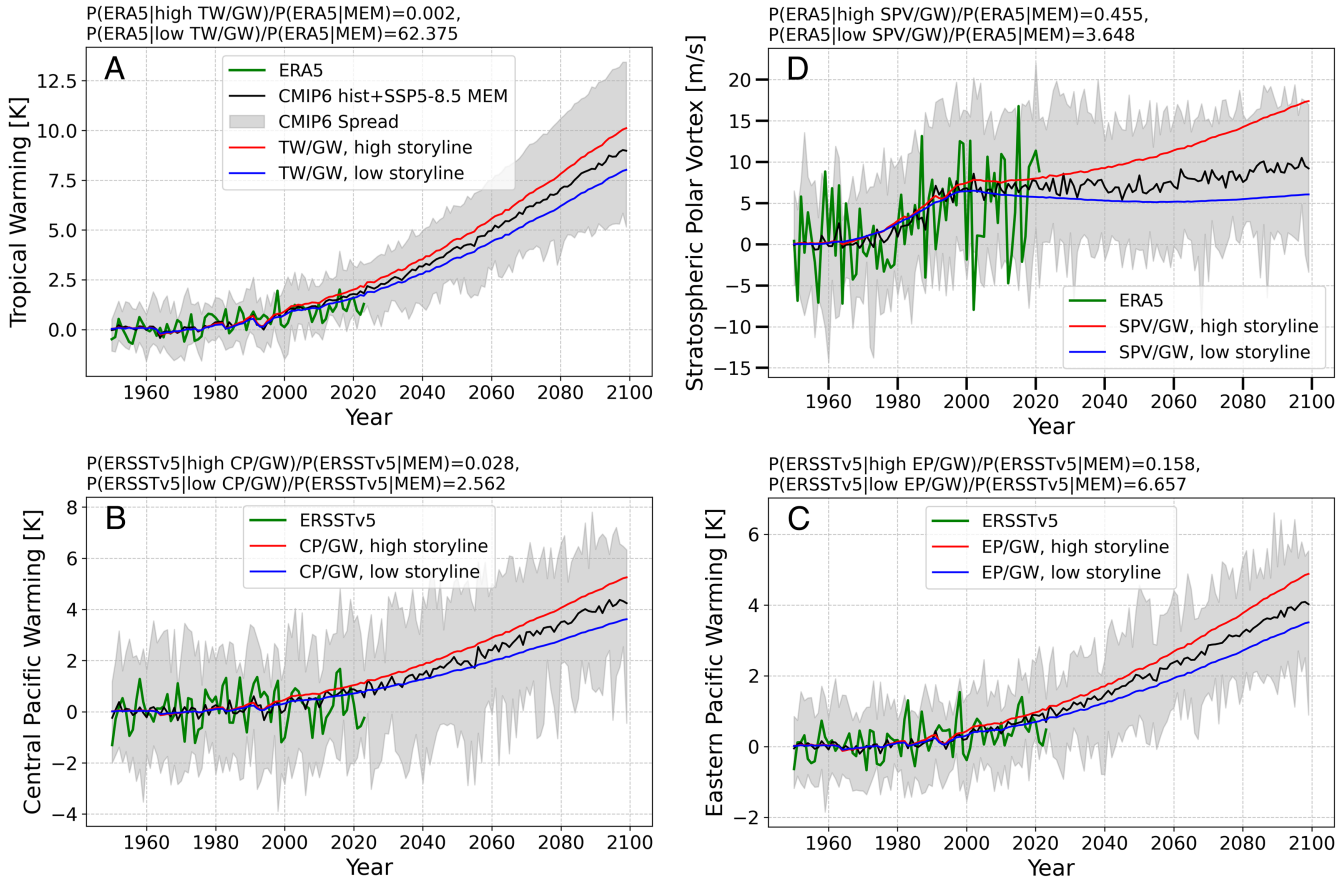

Fig. 4. Storylines of remote driver sensitivity to forcing. (*A*) Tropical Warming (TW) anomalies with respect to the 1950–1979 climatology in spliced (historical+SSP5-8.5) CMIP6 simulations (gray shading), multimodel ensemble mean (MEM), high and low TW storylines (red and blue respectively), and ERA5 data (green). (*B*) Same as (*A*) but for the Stratospheric Polar Vortex (SPV). (*C* and *D*) Same as (*B*) but for Central Pacific warming and Eastern Pacific warming estimated from the ERSSTv5 dataset. The evolution of the remote driver (RD) under a high/low RD storyline is estimated as the product of the storyline coefficient and $\Delta T(t)$ where $\Delta T(t)$ is the MEM global warming time series estimated from the CMIP6 ensemble. The distribution for RDs is shown in *SI Appendix*, Fig. S9 and storyline coefficients are shown in *SI Appendix*, Table S2. The titles in each panel show the Bayes Factor (BF) corresponding to each storyline, that is, the ratio of the probability of observing the ERA5 or ERSSTv5 data given the hypothesis that the climate is following a storyline vs. the probability of observing the same given the hypothesis that the climate is following the MEM. For the estimation of the Bayes Factors see *Materials*.

driver than the MEM. By convention (36), a BF larger than 10 (or smaller than 0.1) indicates strong evidence (38–40) in favor (or against) the hypothesis that a given storyline matches the observed trend better than the MEM, whereas BFs in between can be interpreted as inconclusive. We find that the observed TW is 62 times more likely to have occurred if we followed the low TW storyline (blue line in Fig. 4*A*) compared to the MEM response. The high/low SPV storylines are as good as the MEM in explaining the observed response (BFs between 0.1 and 10). The observed warming in the CP and EP are slightly more likely to have occurred if we were following the low CP and EP storylines, but this conclusion depends on the observational product (*SI Appendix*, Figs. S14 and S15). Thus, while the reanalysis products show evidence in favor of the low TW storylines, the SPV, CP, and EP storylines remain uncertain and the observed trends do not provide enough evidence to constrain the ensemble.

From Explaining to Predicting the Eddy-Driven Jet. In this last section, we use the constrained dynamical storylines to explain and predict EDJ trends. We start by analyzing how models simulate the EDJ in the recent past and near-term future (15 y ahead). Past EDJ trends are represented in the model ensemble. However, we find that the ERA5 trends lie on the edge of the full spread if all simulations are considered and outside the distribution if model means are evaluated before assessing latitude and strength trends (*SI Appendix*, Fig. S16). This is particularly true for the strengthening of the jet. Differences in the models' responses can be recovered with the causal network (*SI Appendix*, Text S2 and Figs. S5–S9). However, the different responses can arise not only from the remote driver spread but also from biases in the $u850$ mean state and variability (*SI Appendix*, Fig. S10), which makes it a challenge to take them at face value.

To leverage our causal model of the EDJ (Fig. 1), we use it to estimate the forced EDJ trends under each dynamical storyline, assuming that the mean state and variability are fixed to those of ERA5 and the only source of uncertainty is the remote driver sensitivity to forcing. This acts as a third constraint on the storyline ensemble. Note that the EDJ responses evaluated for each storyline do not necessarily span the spread around the simulated CMIP6 mean. Instead, they span the uncertainty in the ERA5 EDJ that we can attribute to the uncertainty in the forced remote driver responses, which we estimated from CMIP6 and represented with an ensemble of dynamical storylines in the previous section. Fig. 5 shows the zonal mean and basin jet metrics as described by the CMIP6 ensemble, the ERA5 reanalysis, the attributed component of ERA5 (as in Fig. 2) and an ensemble of EDJ storylines estimated as the linear combination of the storylines of remote driver trends and the causal pathways (*Materials*). We estimate Bayes Factors again to compare the likelihood of observing the previously attributed ERA5 data

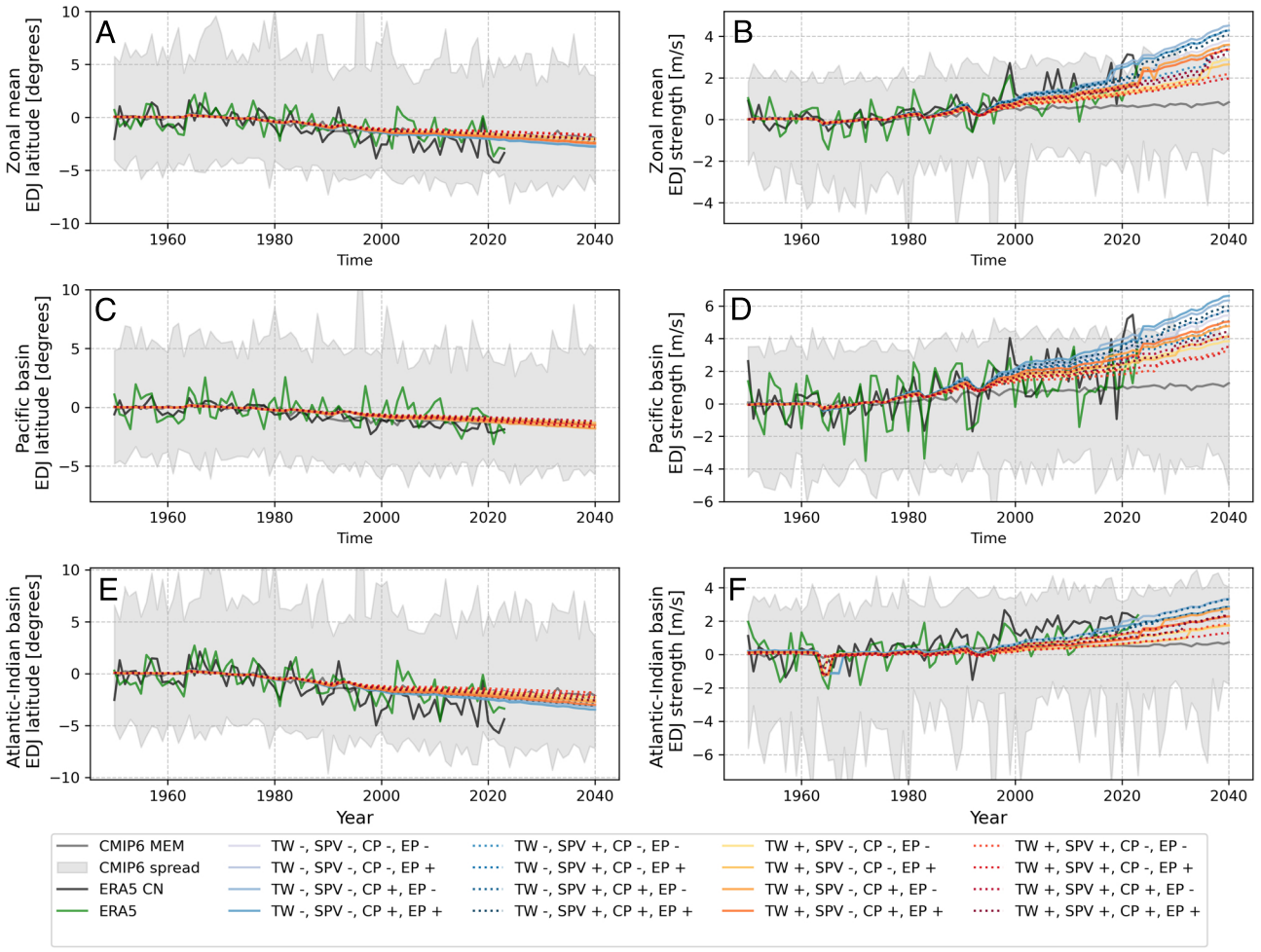

Fig. 5. (*A*) Total spread in the model mean EDJ latitude anomalies with respect to the 1950–1979 climatology are estimated from *u*850 in concatenated (historical+SSP5-8.5) CMIP6 simulations (gray shading), overlaid are the storylines projected until 2040 (color code) and anomalies with respect to the same period estimated from ERA5 reanalysis data (black). The storylines for which we find more evidence are shown with solid lines. (*B*) Same as (*A*) but for EDJ strength. (*C* and *D*) Same as (*A* and *B*) but for the Pacific basin. (*E* and *F*) Same as (*A* and *B*) but for the Atlantic-Indian basin.

under the hypothesis that we are following a given storyline as opposed to the hypothesis of being under the MEM (Fig. 6).

We find that in particular the strengthening of the EDJ in all basins is better explained by any of the proposed storylines compared to the MEM, with larger BFs for almost all storylines (BF $\geq$ 100) and particularly higher BFs for the low TW. Only the latitude shift in the Pacific Basin is better explained by the MEM compared to all the storylines. In summary, all but one EDJ metric is better explained by the storylines than by the MEM (or the storylines are at least equally good). Moreover, the BFs of the latitude and strength metrics in the zonal mean and Atlantic basin confirm that low TW storylines better explain the observed trends.

Fig. 7 shows the spatial pattern of observed wind changes per degree of warming and under the storylines with largest BFs (low TW and two opposite storylines of SPV, CP, and EP warming). Spatially, these storylines present a strong latitude shift in the Atlantic-Indian basin and a strengthening in the Pacific basin, as reported by Waugh et al. (11). The correlation between the patterns is shown in *SI Appendix*, Fig. S20. Note that the NCEP reanalysis (Fig. 7*B*) presents a different spatial response compared to JRA55 (Fig. 7*A*) and ERA5 (Fig. 7*C*) and the response is more zonally symmetric. The strength of the MEM pattern of change per degree of warming (Fig. 7*F*) is much weaker than the storylines that we estimate (Fig. 7 *D* and *E*). Moreover, the zonal asymmetries are not captured by the MEM, but they are captured by our proposed storylines. According to our dynamical storyline prediction, if we continue to follow the storylines for which we found more evidence in the previous section (low TW) the latitude and strength of the EDJ will remain above the values projected by the MEM while remaining inside the projected plume. We did not find sufficient evidence to constrain the uncertainty associated with SPV, CP, and EP.

Discussion

Our approach combining causal networks with storylines of the forced dynamical response has allowed us to explain and predict observed and simulated changes in the EDJ based on well-known relationships between key remote drivers and zonal winds at 850 hPa. It can be understood as complementary to what is known as the fingerprint method, which addresses the question "Has the climate change signal, associated with a particular forcing, emerged?" (41). Storylines represent distinct, physically plausible pathways through which large-scale atmospheric circulation may respond to anthropogenic forcing, acknowledging uncertainties in the precise nature of this response (19, 23). Instead of seeking the emergence of a single, predefined forced

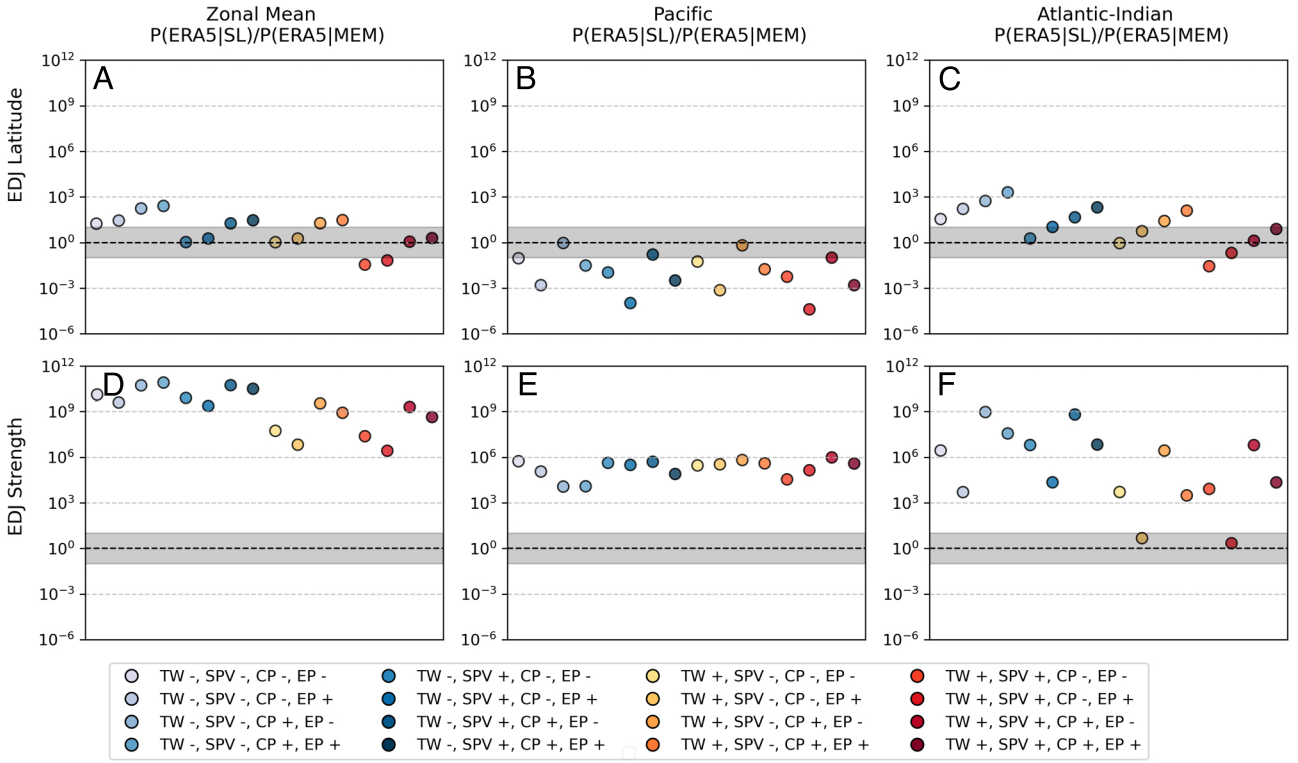

Fig. 6. (*A–C*) Bayes Factor (BF) corresponding to each storyline, plotted on a logarithmic scale. The BF quantifies the ratio of the probability of observing the latitude change in ERA5 under the hypothesis that the climate follows a storyline versus under the hypothesis that it follows the MEM response. A BF $>$ $10(\log_{10}(\mathrm{BF}) \approx 1)$ is interpreted as evidence in favor of the storyline hypothesis (white positive area), while a BF $<$ $0.1(\log_{10}(\mathrm{BF}) \approx -1)$ is interpreted as evidence in favor of the MEM hypothesis (white negative area) (36). Gray areas indicate no significant evidence in favor of either hypothesis. For details on the storyline construction and Bayes Factor computation, see Materials. The corresponding storylines are shown in Fig. 5. (*D–F*) Same as (*A–C*), but for the strength metric.

response—a key limitation of traditional fingerprinting methods due to model uncertainties—we expand the question to ask whether any plausible forced response has emerged and how it can be explained in terms of a small set of driver responses. The estimation of likelihood ratios, the Bayes Factors, is used to compare the agreement of observed remote driver responses with a set of potential responses. This approach reframes the detection problem: Rather than validating a specific model response, we assess whether observed changes align with one or more out of an ensemble of several plausible forced responses. The BF can be estimated for each year of data, adding each year a piece of evidence (*SI Appendix*, Fig. S21). We find that large differences between the storylines that better explain observed trends deviate from the CMIP6 MEM around the year 2000, suggesting a time of emergence of the associated forced response.

The underlying hypothesis behind our causal network (Fig. 1*A*) is that the influence of the remote drivers on the EDJ is the same when the variability of the drivers is generated by internal variability or by anthropogenic forcing. This is justified by other studies that address the sensitivity of the EDJ to the same drivers in different time scales and idealized simulations (12, 18, 28, 31, 42, 43). In addition, a first approach to this question reveals that the causal pathway strengths are stationary in the observed period (44) (*SI Appendix*, Fig. S4). In this respect, we consider the qualitative agreement of the causal maps estimated from reanalysis and piControl and the reproduction of the CMIP6 modeled trends in the concatenated historical+SSP5-8.5 simulations (*SI Appendix*, Fig. S7) as sufficient evidence to work under this hypothesis.

The drivers demonstrate a better representation of EDJ behavior in the South Pacific basin than in the Atlantic-Indian basin, which highlights the need for future investigations focusing into the role of the tropical Atlantic and Indian oceans in driving observed jet strengthening in these regions. Nevertheless, the causal framework allowed us to attribute 50% of the EDJ latitude shift directly to GW and 50% to the remote drivers, and most of the strengthening to the remote drivers (Fig. 2), with the role of GW in the remote driver changes left open in this conditional attribution. Given that EDJ uncertainty is associated not only with remote driver responses to GW but also with transient climate sensitivity and SPV response to ozone depletion, we showed that part of the spread in EDJ responses can be constrained by the observed rate of GW and of the sensitivity of the SPV to ozone depleting substances (Fig. 3). The Bayes Factor estimates suggest that the constrained storylines (regardless of the particular remote driver responses) are more representative of the emerging observed signal than is the CMIP6 MEM (Figs. 4 and 6). Moreover, we find that the CMIP6 MEM appears to underestimate the strengthening trends in the EDJ (Figs. 5 and 7); the proposed storylines offer an alternative to estimating projections of the EDJ. According to this analysis, the observed strengthening EDJ trends do not necessarily result from internal variability, but a predictable signal forced by trends in large scale drivers, particularly in the Pacific basin and the zonal mean. The approach is therefore aligned with other recent work showing that predictable trends could be larger than what models show if taken at face value (45).

In contrast to other dynamical storyline studies where the storylines illustrate the spread in a model ensemble and under a given warming level (23, 31), our approach aims to use the model simulations to understand the past and near-term future, within the context of an observations-based conditional attribution of

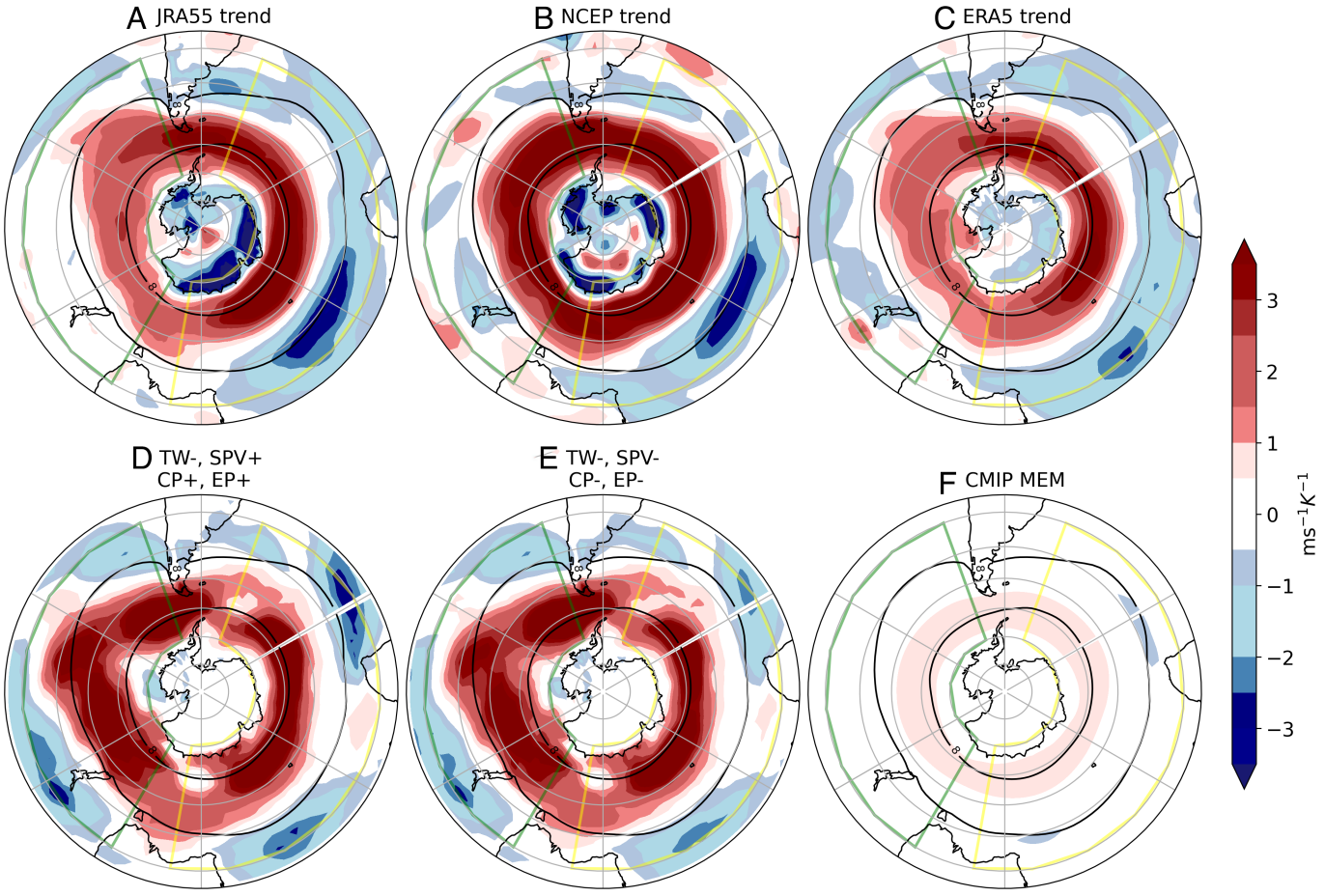

Fig. 7. *u*850 response per degree of warming (ms^{-1} K^{-1}). (*A*–*C*) are estimated from three reanalysis products as the change between the first and last 20 y of the total period for which we use ERA5 data to reconstruct storylines (1950–1973 vs. 2000–2023) and divided by the level of warming in the same period, estimated in the same way. (*D* and *E*) Same as in (*A*–*C*) but for the plausible storylines of climate change related to low TW responses (Eq. **11**), (*F*) CMIP6 MEM response scaled per degree of warming, evaluated in the same way as (*A*–*C*) for each model individually and then averaged to get the ensemble mean.

the EDJ trends. Assumptions behind the proposed storylines are that i) EDJ trends are controlled by the trends in the proposed drivers and their influence is statistically stationary, ii) projections can be constrained to the MEM GW rate and stratospheric response to ozone depletion/recovery. Future work could be directed to develop alternative approaches to near-term estimations that are not conditioned by these assumptions, such as storylines that systematically explore the possibility of remote driver responses changing over time. Given the potential impacts of underestimating the climate response to anthropogenic forcing at the regional scale (4), we find it imperative to use physical understanding to explore possible storylines that are not represented by the latest available CMIP simulations.

Materials

We used the piControl (last 200 y of every simulation), the historical (1900–2014), and the SSP5-8.5 scenarios (2015–2099) from 33 CMIP6 models (46). We work with monthly outputs of zonal winds (ua) at 850 hPa and 50 hPa, surface air temperature (tas), upper tropospheric temperature (ta) at 250 hPa and sea surface temperature (tos). All model outputs are interpolated into a common grid of 2.5° using the ESMF area weighted scheme implemented in the Python Iris package. The downloading and preprocessing of the data was done using ESMValTool (47). For the estimation of the remote driver responses, we averaged all the available ensemble members available for each model (model mean) to reduce the influence of internal variability. When we refer to the multimodel ensemble mean, we refer to the average of the model means. The list of models and ensemble members used can be found in Dataset S1.

To investigate the historical period we used the HadCRUT5 dataset (48) for global surface temperature, three different sea surface temperature (SST) observational datasets: the Hadley Centre Sea Ice and SST v.1.1 (HadISSTv1) (49), the Centennial In Situ Observation-Based Estimates of the Variability of SST and Marine Meteorological Variables v.2 (COBEv2) (49) and the National Oceanic and Atmospheric Administration Extended Reconstructed SST v.5 (ERSSTv.5) (50) and three reanalysis: Japanese 55-y Reanalysis (JRA-55) (51), NCEP/NCAR reanalysis (52) and the extended ERA5 reanalysis (53). We mostly present results from ERA5, as this is the reanalysis which provides the longest time series, but the results are not sensitive to the choice of reanalysis and we show results for JRA55 and NCEP in *SI Appendix*. The data from the reanalyses were interpolated into the common 2.5° grid for all the analyses.

Eddy-Driven Jet Metrics. The latitude of the EDJ was calculated as the centroid of the zonal wind at 850 hPa between 30 and 70S (54). We quantified the latitude and strength of the zonally averaged EDJ and over the Pacific and Atlantic-Indian basins following ref. 11, which showed that the observed trends in the Pacific basin have different trends than the zonal mean due to the influence of the tropical Pacific. The longitude bands we used were 210-80W for the Pacific basin and 40W-120E for the Atlantic-Indian basin.

$$\overline{\lambda} = \int_{70S}^{30S} \frac{\lambda[u(\lambda)]^2}{[u(\lambda)]^2} d\lambda \qquad [1]$$

Wind strength is the wind strength at the EDJ latitude averaged over the different basins.

Causal Inference. We first proposed a causal model (Fig. 1*A*) of the EDJ based on the revision of published literature as interpreted by our expert judgment. In this causal model, internal variability and anthropogenic forcing are exogenous variables, and the remote drivers and the zonal winds (or metrics of the EDJ) in the SH are endogenous variables (55). To quantify causal pathways between the remote driver and the EDJ we fit a series of multiple linear regression (MLR) models where the covariates are the remote drivers and the target variable is either 1) the latitude or strength of the EDJ (which yields a scalar estimation for each metric, *SI Appendix*, Table S1) or 2) the zonal wind at all grid cells in the Southern Hemisphere (which yields a set of causal maps, *SI Appendix*, Table S1).

The MLR model for a (scalar) jet metric is

$$EDJ'_{lat} = \sum_i \beta_i^{lat} RD'_i(t) + \epsilon_{lat}(t) \quad [2]$$

$$EDJ'_{str} = \sum_i \beta_i^{str} RD'_i(t) + \epsilon_{str}(t) \quad [3]$$

where $EDJ'_{metric}(t)$ is the metric standardized anomaly , RD'_i(t) are the standardized anomalies of the remote drivers and ϵ_{metric}(t) are assumed Gaussian errors. The coefficients β^i_{metric} are estimated with an ordinary multivariate least squares algorithm implemented in the Python Stats package. To evaluate the spatial influence of the drivers on the zonal winds we use the same MLR model, but in this case fitted to each grid cell:

$$u850'(x,t) = \sum_i \beta_i(x) RD'_i(t) + \epsilon(x,t), \quad [4]$$

where $u850'$ are the standardized anomalies of the seasonal average (December–February, DJF) of zonal winds and x represents grid cells and the apostrophe indicates that the variable is standardized with respect to the mean and SD of the whole period (1950–2023 for ERA5, 1950–2023 for JRA55, and 1958–2023 for NCEP). Estimated causal maps, $\hat{\beta_i}(x)$, are standardized responses of zonal winds to one SD in the time series of the remote driver and can be converted to physical units by multiplying them by the SD of the winds at each grid cell.

In both the metric and spatial MLR, the RD'_i(t) are standardized anomalies of:

- TW, evaluated as the zonal average of temperature at 200 hPa between 15S and 15N in DJF,
- SPV strength in October–November, evaluated as the zonal mean of the zonal wind strength at 50 hPa between 50S and 60S,
- The central Pacific (CP) and eastern Pacific (EP) sea surface temperature in DJF, evaluated as the sea surface temperature averaged over the boxes [5N-5S,180-250E] and [0-10S,260-280E] respectively in DJF and
- Global mean surface temperature (GW), the area weighted global average of surface air temperature in DJF.

Note that this approach does not exclude the possibility that causal links exist between the drivers, these are possible and certainly exist, for example in the case of CP → TW (56). However, since the purpose of this article is not to describe the full network involving these drivers, we do not quantify these links. We rather use the estimated pathways to make estimates of $u850$ based on observed (Fig. 2) or proposed storylines (Figs. 4–6) for the remote drivers. The MLR framework ensures that by including all the drivers in the regression, the correct links are estimated (34, 55). We do not use the first 10 y of ERA5 data since it is reported that over the SH this early period is mainly statistical and a cold bias has been revealed in the stratosphere (57). The last value of the time series is December (2023) and January–February (2024).

Constraint on the GW Rate and SPV Sensitivity to Ozone Depleting Substances. To evaluate the response of the SPV to external forcing, we perform a multiple linear regression of SPV anomalies onto global warming (GW) and equivalent effective stratospheric chlorine (EESC), following the approach of ref. 21. The regression model is given by

$$\Delta\mathrm{SPV}(t) = a\,\Delta\mathrm{EESC}(t) + b\,\Delta\mathrm{GW}(t) + \epsilon, \quad [5]$$

where ΔSPV(t) is the anomalous SPV index (e.g., zonal-mean zonal wind at 60°S, 10 hPa), ΔEESC(t) is the polar EESC time series based on mid-latitude mixing ratios from the WMO Scientific Assessment of Ozone Depletion (2014) (58), and ΔGW(t) represents the global-mean surface temperature anomaly time series relative to 1950–1979. All time series are anomalies are computed with respect to a 1950–1979 climatology.

The regression coefficients are computed separately for each CMIP6 model over two periods: 1) the historical-to-present interval (1979–2023) and 2) the full available time span (1950–2100). The diagnosed sensitivity of SPV to EESC forcing (a in Eq. **5**) is compared between the historical and future periods across the CMIP6 ensemble. This comparison is visualized via a scatter plot that contrasts SPV sensitivity to EESC in 1979–2023 vs. 2080–2100 (Fig. 3*A*). The observed estimate from ERA5 is shown alongside the model distribution, and the relationship is benchmarked against a 1:1 line to assess potential shifts in SPV response under future conditions.

To quantify the rate of GW across the CMIP6 ensemble, we analyze model-specific time series of global surface temperature anomalies relative to the 1950–1979 mean. For each model, temperature anomalies are fit with a second-order polynomial $T(t) = at^2 + bt + c$ over two periods: 1950–2020 and 1950–2040. The instantaneous rate of warming is then computed as the derivative of the fitted polynomial:

$$\frac{dT}{dt} = 2a\,t + b, \quad [6]$$

evaluated at the midpoint of each respective period (1985 for 1950–2020 and 1995 for 1950–2040). This provides an estimate of the warming rate (in °C/year) under historical and near-future conditions. Observational warming rates are calculated using a quadratic fit to global DJF temperature anomalies from HadCRUT5, and the MEM rate is similarly computed from the average model temperature trajectory.

Storylines of Remote Driver Responses. The responses of the TW, CP, and EP are estimated as the climatological change (1940–1969 vs. 2070–2099) in each of the drivers as defined in the last section scaled by the global mean surface temperature difference in the same period. The response of the SPV to forcing is estimated by regression of the SPV index onto GW and equivalent effective stratospheric chlorine as in Eq. **5**.

Bayes Factors. The probability of observing the trends of the last seven decades under each hypothesis (or storyline, H_1) can be contrasted to the probability of observing the data if the correct estimate for the remote driver responses were to be the MEM (H_0) (39). The ratio of these two probabilities is the Bayes Factor: BF = P(data|H_1) / P(data|H_0).

Each of the hypothesis H_1 is, by definition, a linear model of the driver sensitivity to GW:

$$\Delta RD_i^{sl}(t) = b_{sl}\Delta GW(t) + \epsilon, \quad [7]$$

where b_{sl} is the storyline coefficient (sl can be high or low; see *SI Appendix*, Table S2) and $\Delta GW(t)$ is the MEM $\Delta GW(t)$ evolution. Except for SPV, for which the storylines are estimated as

$$\Delta SPV^{sl}(t) = a\Delta EESC(t) + b_{sl}\Delta GW(t)\epsilon, \quad [8]$$

where a is the MEM SPV response to EESC (0.0018 $ms^{-1}ppm^{-1}$) and b_{sl} is the storyline coefficient for the storylines (H_1). For the alternative hypothesis (H_0), the RD time series is estimated as the MEM response. We assume that the year-to-year variability behaves as Gaussian noise, which we consider valid given that we checked that the detrended time series of these variables present no significant autocorrelation (*SI Appendix*, Fig. S22). If the noise is Gaussian, the

probabilities P(data|H_0) and P(data|H_1) can also be modeled with the Gaussian distribution:

$$P(\Delta RD_{obs}|H, b) = \frac{1}{\sqrt{2\pi}\sigma} \exp\left[\frac{\sum_{k=1}^{N}((\Delta RD_{obs}(t_k) - \Delta RD_{sl}(t_k))^2)}{2\sigma^2}\right] \quad [9]$$

$$= \frac{1}{\sqrt{2\pi}\sigma} \exp\left[-\left(\frac{SSE}{2\sigma^2}\right)\right], \quad [10]$$

where σ^2 is the variance of the year-to-year variability in the observed time series of each detrended remote driver anomaly (38, 40).

Reconstruction of *u*850 Storylines. To estimate the evolution of $u850_{sl}(x,t)$ under each storyline (*sl*) we consider the mean state and variability to be that of ERA5 ($\overline{u850_{ERA5}(x)}$ and $\sigma_{u850_{ERA5}}(x)$) and estimate the forced trends at each grid point using the causal maps $\beta_i(x)$ estimated from ERA5 and the time series of each remote driver time series corresponding to each storyline $RD_i^{sl}(t)$:

$$u850'_{sl}(x,t) = \overline{u850_{ERA5}(x)} + \sum_i \hat{\beta_i}(x)\sigma_{u850_{ERA5}}(x)RD_i'^{sl}(t) + \epsilon(x,t), \quad [11]$$

where *sl* represents the storyline coefficient (high/low). The time series of each remote driver is estimated as for the Bayes Factor calculation detailed above, where b_{sl} is the high/low value of the remote driver sensitivity to global warming (*SI Appendix*, Fig. S9 and Table S1). Given that we do not evaluate storylines of different GW rates, the MEM $\Delta GW(t)$ evolution is used to estimate the GW contribution. The Bayes Factor analysis in Fig. 6 is performed in the same way as for the RDs, but with the EDJ metrics.

Data, Materials, and Software Availability. Code is available via a Github repository. All the data used for this study are publicly available. Previously published data were used for this work (46, 48, 50–53).

ACKNOWLEDGMENTS. We want to thank the reviewers for their very constructive comments, which have greatly contributed to shape the article and Pep Cos for his help with the use of ESMValTool. J.M. was funded by a PhD grant from the Consejo Nacional de Investigaciones Científicas y Técnicas (CONICET) during parts of this work and Funded by the Saxon State Ministry for Science, Culture and Tourism (SMWK)–[3-7304/44/4-2023/8846]. T.G.S. and M.K. acknowledge funding from the European Commission Horizon 2020 project XAIDA (Extreme Events: Artificial Intelligence for Detection and Attribution), Grant Agreement No. 101003469. M.K. further acknowledges funding from the Horizon Europe project EXPECT (Towards an Integrated Capability to Explain and Predict Regional Climate Changes), Grant Agreement No. 101137656. M.O. and C.S.V. were funded by the Agencia Nacional de Promoción Científica y Tecnológica (grant no. PICT-2021-GRF-TI-00498), the Universidad de Buenos Aires (grant no. 20020220100075BA), and the Consejo Nacional de Investigaciones Científicas y Técnicas (CONICET) (grant no. PIP11220200102038CO).

Author affiliations: [a]Leipzig Institute for Meteorology, Leipzig 04103, Germany; [b]Department of Meteorology, University of Reading, Reading RG6 6ET, United Kingdom; [c]Jülich Supercomputing Centre, Forschungszentrum Jülich, Jülich 52428, Germany; [d]Departamento de Ciencias de la Atmósfera y los Océanos, Facultad de Ciencias Exactas y Naturales, Universidad de Buenos Aires, Buenos Aires C1428EGA, Argentina; [e]Centro de Investigaciones del Mar y la Atmósfera, Consejo Nacional de Investigaciones Científicas y Técnicas, Universidad Nacional de Buenos Aires, Buenos Aires C1428EGA, Argentina; and [f]Instituto Franco Argentino sobre estudios de Clima y sus impactos (IFAECI-UMI3351), Centre National de la Recherche Scientifique, Buenos Aires C1428EGA, Argentina

Author contributions: J.M. and T.G.S. designed research; J.M. performed research; J.M., T.G.S., M.O., C.S.V., and M.K. contributed new reagents/analytic tools; J.M. analyzed data; J.M. and C.S.V. interpretation; T.G.S., M.O., and M.K. interpretation, editing; and J.M. wrote the paper.

1. J. Mindlin *et al.*, Storyline description of Southern Hemisphere midlatitude circulation and precipitation response to greenhouse gas forcing. *Clim. Dyn.* **54**, 4399–4421 (2020).
2. H. Nguyen *et al.*, Variability of the extent of the Hadley circulation in the Southern Hemisphere: A regional perspective. *Clim. Dyn.* **50**, 129–142 (2018).
3. T. Woollings, M. Drouard, C. H. O'Reilly, D. M. H. Sexton, C. McSweeney, Trends in the atmospheric jet streams are emerging in observations and could be linked to tropical warming. *Commun. Earth Environ.* **4**, 125 (2023).
4. T. A. Shaw *et al.*, Emerging climate change signals in atmospheric circulation. *AGU Adv.* **5**, e2024AV001297 (2024).
5. D. W. J. Thompson, S. Solomon, Interpretation of recent Southern Hemisphere climate change. *Science* **296**, 895–899 (2002).
6. J. M. Arblaster, G. A. Meehl, Contributions of external forcings to southern annular mode trends. *J. Clim.* **19**, 2896–2905 (2006).
7. S. Son *et al.*, Impact of stratospheric ozone on Southern Hemisphere circulation change: A multimodel assessment. *J. Geophys. Res. Atmos.* **115**, 2010JD014271 (2010).
8. S. Lee, S. B. Feldstein, Detecting ozone- and greenhouse gas-driven wind trends with observational data. *Science* **339**, 563–567 (2013).
9. A. Banerjee, J. C. Fyfe, L. M. Polvani, D. Waugh, K. L. Chang, A pause in Southern Hemisphere circulation trends due to the Montreal Protocol. *Nature* **579**, 544–548 (2020).
10. A. Ossó *et al.*, Advancing our understanding of eddy-driven jet stream responses to climate change - A roadmap. *Curr. Clim. Chang. Rep.* **11**, 2 (2024).
11. D. W. Waugh, A. Banerjee, J. C. Fyfe, L. M. Polvani, Contrasting recent trends in Southern Hemisphere westerlies across different ocean basins. *Geophys. Res. Lett.* **47**, e2020GL088890 (2020).
12. D. Yang, J. M. Arblaster, G. A. Meehl, M. H. England, The role of coupled feedbacks in the decadal variability of the Southern Hemisphere eddy-driven jet. *J. Geophys. Res. Atmos.* **126**, e2021JD035023 (2021).
13. P. J. Kushner, I. M. Held, T. L. Delworth, Southern Hemisphere atmospheric circulation response to global warming. *J. Clim.* **14**, 2238–2249 (2001).
14. J. H. Yin, A consistent poleward shift of the storm tracks in simulations of 21st century climate. *Geophys. Res. Lett.* **32**, 2005GL023684 (2005).
15. G. K. Vallis, P. Zurita-Gotor, C. Cairns, J. Kidston, Response of the large-scale structure of the atmosphere to global warming. *Q. J. R. Meteorol. Soc.* **141**, 1479–1501 (2015).
16. G. Chen, I. M. Held, Phase speed spectra and the recent poleward shift of Southern Hemisphere surface westerlies. *Geophys. Res. Lett.* **34**, 2007GL031200 (2007).
17. E. P. Lim, I. Simmonds, Effect of tropospheric temperature change on the zonal mean circulation and SH winter extratropical cyclones. *Clim. Dyn.* **33**, 19–32 (2009).
18. A. H. Butler, D. W. J. Thompson, R. Heikes, The steady-state atmospheric circulation response to climate change-like thermal forcings in a simple general circulation model. *J. Clim.* **23**, 3474–3496 (2010).
19. T. A. Shaw, Mechanisms of future predicted changes in the zonal mean mid-latitude circulation. *Curr. Clim. Chang. Rep.* **5**, 345–357 (2019).
20. T. J. Bracegirdle *et al.*, Twenty first century changes in Antarctic and Southern Ocean surface climate in CMIP6. *Atmos. Sci. Lett.* **21**, e984 (2020).
21. J. Mindlin, T. G. Shepherd, C. Vera, M. Osman, Combined effects of global warming and ozone depletion/recovery on Southern Hemisphere atmospheric circulation and regional precipitation. *Geophys. Res. Lett.* **48**, e2021GL092568 (2021).
22. T. G. Shepherd, Atmospheric circulation as a source of uncertainty in climate change projections. *Nat. Geosci.* **7**, 703–708 (2014).
23. G. Zappa, T. G. Shepherd, Storylines of atmospheric circulation change for European regional climate impact assessment. *J. Clim.* **30**, 6561–6577 (2017).
24. T. G. Shepherd, Storyline approach to the construction of regional climate change information. *Proc. R. Soc. A Math. Phys. Eng. Sci.* **475**, 20190013 (2019).
25. B. J. Harvey, P. Cook, L. C. Shaffrey, R. Schiemann, The response of the Northern Hemisphere storm tracks and jet streams to climate change in the CMIP3, CMIP5, and CMIP6 climate models. *J. Geophys. Res. Atmos.* **125**, e2020JD032701 (2020).
26. C. Junquas, C. S. Vera, L. Li, H. Le Treut, Impact of projected SST changes on summer rainfall in southeastern South America. *Clim. Dyn.* **40**, 1569–1589 (2013).
27. N. J. Byrne, T. G. Shepherd, Seasonal persistence of circulation anomalies in the Southern Hemisphere stratosphere and its implications for the troposphere. *J. Clim.* **31**, 3467–3483 (2018).
28. P. Ceppi, T. G. Shepherd, The role of the stratospheric polar vortex for the austral jet response to greenhouse gas forcing. *Geophys. Res. Lett.* **46**, 6972–6979 (2019).
29. D. Yang *et al.*, Role of tropical variability in driving decadal shifts in the Southern Hemisphere summertime eddy-driven jet. *J. Clim.* **33**, 5445–5463 (2020).
30. R. Ghosh, T. G. Shepherd, Storylines of Maritime Continent dry period precipitation changes under global warming. *Environ. Res. Lett.* **18**, 034017 (2023).
31. J. Mindlin, C. S. Vera, T. G. Shepherd, M. Osman, Plausible drying and wetting scenarios for summer in southeastern South America. *J. Clim.* **36**, 7973–7991 (2023).
32. E. Baulenas, G. Versteeg, M. Terrado, J. Mindlin, D. Bojovic, Assembling the climate story: Use of storyline approaches in climate-related science. *Glob. Chall.* **7**, 2200183 (2023).
33. A. Hall, P. Cox, C. Huntingford, S. Klein, Progressing emergent constraints on future climate change. *Nat. Clim. Chang.* **9**, 269–278 (2019).
34. M. Kretschmer *et al.*, Quantifying causal pathways of teleconnections. *Bull. Am. Meteorol. Soc.* **102**, E2247–E2263 (2021).
35. E. A. Barnes, D. L. Hartmann, D. M. W. Frierson, J. Kidston, Effect of latitude on the persistence of eddy-driven jets. *Geophys. Res. Lett.* **37**, 2010GL043199 (2010).
36. A. M. Ellison, An introduction to Bayesian inference for ecological research and environmental decision-making. *Ecol. Appl.* **6**, 1036–1046 (1996).
37. S. Shikano, Hypothesis testing in the bayesian framework. *Swiss Polit. Sci. Rev.* **25**, 288–299 (2019).
38. M. Kretschmer, G. Zappa, T. G. Shepherd, The role of Barents-Kara sea ice loss in projected polar vortex changes. *Weather. Clim. Dyn.* **1**, 715–730 (2020).
39. T. G. Shepherd, Bringing physical reasoning into statistical practice in climate-change science. *Clim. Chang.* **169**, 2 (2021).

40. X. Shen, M. Kretschmer, T. G. Shepherd, A forensic investigation of climate model biases in teleconnections: The case of the relationship Between ENSO and the northern stratospheric polar vortex. *J. Geophys. Res. Atmos.* **129**, e2024JD041252 (2024).
41. K. Hasselmann, "On the signal-to-noise problem in atmospheric response studies" in *Meteorology Over the Tropical Oceans*, D. B. Shaw, Ed. (Royal Meteorological Society, Bracknell, 1979), pp. 251–259.
42. E. Saggioro, T. G. Shepherd, Quantifying the timescale and strength of Southern Hemisphere intraseasonal stratosphere-troposphere coupling. *Geophys. Res. Lett.* **46**, 13479–13487 (2019).
43. R. S. Williams *et al*., Future Antarctic climate: Storylines of midlatitude jet strengthening and shift emergent from CMIP6. *J. Clim.* **37**, 2157–2178 (2024).
44. Y. Tian *et al*., Historical changes in the Causal Effect Networks of compound hot and dry extremes in central Europe. *Commun. Earth Environ.* **5**, 764 (2024).
45. D. M. Smith *et al*., Mitigation needed to avoid unprecedented multi-decadal North Atlantic Oscillation magnitude. *Nat. Clim. Chang.* **15**, 403–410 (2025).
46. V. Eyring *et al*., Overview of the Coupled Model Intercomparison Project Phase 6 (CMIP6) experimental design and organization. *Geosci. Model. Dev.* **9**, 1937–1958 (2016).
47. V. Eyring *et al*., Earth System Model Evaluation Tool (ESMValTool) v2.0 - an extended set of large-scale diagnostics for quasi-operational and comprehensive evaluation of Earth system models in CMIP. *Geosci. Model. Dev.* **13**, 3383–3438 (2020).
48. C. P. Morice *et al*., An updated assessment of near-surface temperature change from 1850: The HadCRUT5 data set. *J. Geophys. Res. Atmos.* **126**, e2019JD032361 (2021).
49. D. P. Schneider, C. Deser, J. Fasullo, K. E. Trenberth, Climate data guide spurs discovery and understanding. *EOS Trans. Am. Geophys. Union* **94**, 121–122 (2013).
50. B. Huang *et al*., Extended Reconstructed Sea Surface Temperature, Version 5 (ERSSTv5): Upgrades, Validations, and Intercomparisons. *J. Climate* **30**, 8179–8205 (2017).
51. S. Kobayashi *et al*., The JRA-55 reanalysis: General specifications and basic characteristics. *J. Met. Soc. Japan* **93**, 5–48 (2015).
52. E. Kalnay *et al*., The NCEP/NCAR 40-year reanalysis project. *Bull. Am. Meteorol. Soc.* **77**, 437–471 (1996).
53. H. Hersbach *et al*., The ERA5 global reanalysis. *Q. J. R. Meteorol. Soc.* **146**, 1999–2049 (2020).
54. P. Ceppi, G. Zappa, T. G. Shepherd, J. M. Gregory, Fast and slow components of the extratropical atmospheric circulation response to CO2 forcing. *J. Clim.* **31**, 1091–1105 (2018).
55. J. Pearl, M. Glymour, N. P. Jewell, *Causal Inference in Statistics: A Primer* (Wiley, Chichester, West Sussex, 2016).
56. L. Li *et al*., Response of upper tropospheric water vapor to global warming and ENSO. *Sci. Rep.* **14**, 5995 (2024).
57. C. Soci *et al*., The ERA5 global reanalysis from 1940 to 2022. *Q. J. R. Meteorol. Soc.* **150**, 4014–4048 (2024).
58. P. A. Newman, J. S. Daniel, D. W. Waugh, E. R. Nash, A new formulation of equivalent effective stratospheric chlorine (EESC). *Atmos. Chem. Phys.* **7**, 4537–4552 (2007).